

## NON-LINEAR-TRANSFORMATION-FIELD TO BUILD MOVING MESHES FOR PATIENT SPECIFIC BLOOD FLOW SIMULATIONS

Ramiro Moreno\*†, Franck Nicoud ‡, Louis Veunac †, Hervé Rousseau †

† Radiology Department, CHU of Rangueil, Toulouse, France  
\* moreno.r@chu-toulouse.fr

‡ University Montpellier II – CNRS UMR 5149 I3M, CC 051, Montpellier, France

**Key Words:** Moving Mesh, Fluid to wall interaction, Magnetic Resonance Imaging, Aorta.

**Abstract.** *Hemodynamic factor in the thoracic aorta is believed to play an important role in the initiation and the progress of endovascular injuries. Most reported studies are dealing with averaged physiological geometries and rigid arterial boundaries. However, for diseases such as the aortic dissection, the geometrical changes are very patient-specific and the wall motions over the cardiac cycle influence the blood flow drastically. There is a need to generalize the patient-specific studies where the actual inlet/outlet boundary conditions and wall motions are accounted for. But in the most general approach, the geometrical changes during the cardiac cycle result from the coupled fluid-structure interaction problem.*

*This path is very challenging because the density of blood and tissues are of the same order, the rheology of the vessels is far from well understood and because the actual answer depends on the interaction of the arteries with the surrounding organs. Another option is to study the respond of the blood flow submitted to prescribed wall motions and geometry changes.*

*Our study propose a method to build patient-specific geometric data and boundary conditions for unsteady CFD runs with variable meshes valid over the cardiac cycle. We develop a specific MRI protocol in order to extract the full geometric data at several phases over the cardiac cycle. Hemodynamic boundary conditions (velocity inlet and pressure outlets) were acquired by means of anothers two sequences into the same MRI device, a velocity-encoded MR imaging<sup>1</sup> for the velocity inlet profile and a pressure-gradients-encoded imaging<sup>2</sup> for the outlets. Static vascular surfaces have been extracted by means of Level Set methods<sup>3</sup>, after developing a noise reduction strategy called 'selective blurring filter'<sup>4</sup>. Finally, the mesh movement has been imposed to the static mesh according to dynamic MRI sequence by means of a non linear transformation field, computed from dynamic vascular images by means of bayesian algorithm<sup>5</sup>. The proposed approach permits the computation of the blood flow under realistic in vivo, time evolving conditions. It is much simpler than the full coupled fluid-structure problem and has the potential to provide a better picture of the specific hemodynamic status. Insights about the physiopathology of some arterial disease are also expected.*

## 1 INTRODUCTION

Risk factors for cardiovascular disease (hypertension and high cholesterol) and their role have been identified, but cannot explain the observed localised occurrence and the progression of the disease (stenosis, aneurysm). Although cardiovascular disease is clearly multi-factorial, it has been shown that deviations of the normal velocity field (changes in wall shear stress) play a key role. The mechanical load induced by the fluid on atherosclerotic plaques and their composition is of utmost importance for predicting future rupture in order to prevent ischaemic events.

Currently available techniques such as Computed Tomography, Magnetic Resonance Imaging and Ultrasound do not allow accurate determination of the complex velocity distribution and biomechanical load on the arterial wall. Access to patient-specific detailed flow in representative stages of the arterial disease is of key importance to understanding the flow and wall stress related aetiology of the disease or the intimal dissection phenomena development in thoracic aorta.

Today there is not any doubt that medical imaging is an essential tool for the comprehension of cardiovascular diseases.

Computational Fluid Dynamics (CFD) simulations provide an extremely detailed analysis of the flow field and the fluid shear stress to very high accuracy. New advances in simulation techniques could make a significant contribution to a better quantitative knowledge of the biomechanical condition of the arteries and lead to a new understanding via deepened insights into these conditions. The new simulations can potentially be used for prediction of plaque and aneurysm rupture, as well as for guiding treatment decisions by predicting the outcome of surgery or interventional gesture.

There are three key challenges for the breakthroughs needed to enable the application of the fluid-to-wall interaction for future clinical practice : The dynamic vascular geometry needs to be determined from medical images in a robust fashion. The arterial flow rates and pressure levels at the inlet and outlet of the simulated region need to be determined from patient-specific data. Finally, the Navier–Stokes equations will be able to solve numerically with an appropriate finite-element-based method which handles ECG time-dependent geometries.

This paper proposes a new geometrical method where moving mesh and dynamic anatomical data follow the same spatial deformation field during the cardiac cycle. It also proposes an MRI protocol to setup boundary conditions for realistic CFD runs.

## 2 THEORY

This chapter is about warping vascular images of one subject in order to built time evolution of a moving mesh based on the real spatial deformations. A high dimensional model is used, whereby a finite element approach is employed to estimate translation at the location of each voxel in the template image. This model was initially presented by John Ashburner<sup>5</sup> to brain image processing dedicated to computational neuroanatomy.

Considering the deformation field that transform diastolic image  $d$  to systolic image  $s$ . The two fields that map from  $d$  to  $s$ , and from  $s$  to  $d$  can be combined in order to map from  $d$  to  $s$  and then back to  $d$ . If the transformations are perfect, then the resulting deformation should be uniformly zero. Any deviations must be due to transformations errors. The fundamental assumption is made that the probability of stretching a (voxel) by a factor of  $n$  is the same as the probability of shrinking this ( $n \times$  voxel) by a factor of  $n^{-1}$ . For example, a deformation that stretches one voxel in the source image to fit two voxels in the template, should incur the same penalty as the contraction of two voxels to fit one template voxel. In order to compute these potentials in 2D, the pixels of the template image ( $s$ ) are considered as being on a

regular grid, with unit spacing between them, as shown in Figure 1, where a triangular mesh connects the pixel centers. Within each triangle, there is assumed to be a uniform affine mapping between the images. If the co-ordinates of the vertices of an undeformed triangle are  $(x11; x21)$ ,  $(x12; x22)$  and  $(x13; x23)$ , and if they map to co-ordinates  $(y11; y21)$ ,  $(y12; y22)$  and  $(y13; y23)$  respectively, then the 3x3 affine mapping (M) can be obtained by :

$$M = \begin{bmatrix} m_{11} & m_{12} & m_{13} \\ m_{21} & m_{22} & m_{23} \\ 0 & 0 & 1 \end{bmatrix} = \begin{bmatrix} y_{11} & y_{12} & y_{13} \\ y_{21} & y_{22} & y_{23} \\ 1 & 1 & 1 \end{bmatrix} \begin{bmatrix} x_{11} & x_{12} & x_{13} \\ x_{21} & x_{22} & x_{23} \\ 1 & 1 & 1 \end{bmatrix}^{-1} \quad (1)$$

The Jacobian matrix (J) of this affine mapping is simply obtained from matrix M by :

$$J = \begin{bmatrix} m_{11} & m_{12} \\ m_{21} & m_{22} \end{bmatrix} \quad (2)$$

The penalty for distorting each of these triangles is derived from its Jacobian matrix. By using singular value decomposition, J can be decomposed into two unitary matrices (U and V) and a diagonal matrix (S), such that  $J=USV^T$ . The unitary matrices simply represent rotations, and are therefore not important to the penalty function. Diagonal matrix S contains the singular values, and these represent relative stretching in orthogonal directions. The determinant of J ( $|J|$ ) represents relative volume changes, and is the product of the singular values. A suitable prior potential function should preserve a one to one mapping between  $d$  and  $s$ , by constraining the determinants of the Jacobian matrices to be positive.

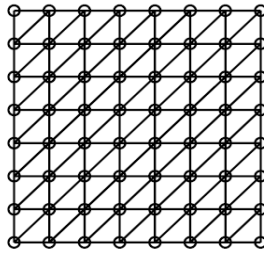


Figure 1: In 2D, template image ( $s$ ) is divided into a triangular mesh, lines connect the center of each pixel, the boundaries are fixed so that the deformation at edges is always zero.

Length and volume changes should have similar distributions. A suitable form for this function is based upon the diagonal elements of S being drawn from a log-normal distribution. The penalty per unit area is therefore (3) where  $\lambda$  is a “regularisation parameter”. Each triangular patch has an area of 1/2 pixel, and it will have an area of  $|J|=2$  pixels when mapped to the space of image  $d$ . The total area affected by the penalty in both the template and source images is therefore  $(1 + |J|)=2$ , so the penalty for each triangle becomes  $h$  and the prior potential  $H$  over the whole image is based on the sum of the potentials for each of the  $I$  triangle.

$$\lambda \log(s_{11})^2 + \lambda \log(s_{22})^2 \quad (3)$$

$$h = \lambda(1 + |J|) \cdot (\log(s_{11})^2 + \log(s_{22})^2) / 2$$

$$H(Y) = \sum_{i=1}^I h_i$$

The transformation is achieved by iteratively matching the images while simultaneously trying to maximise the smoothness of the deformations. Bayesian statistics are used to incorporate this smoothness into the transformation, and a method of optimisation is used for finding the maximum a posteriori (MAP) estimate of the parameters. Bayes theorem can be

written as (4) where  $Y$  are the parameters describing the deformation, and  $b$  are the images to be matched. The estimate determined here is the value of  $Y$  that maximises  $p(Y|b)$ . Figure 2 illustrates a test case of non-linear deformation between a case and a disc.

$$p(Y|b) \propto p(b|Y)p(Y) \quad (4)$$

In 3D, the volume of the template phase image is divided into a mesh of irregular tetrahedra, where the vertices are centered on the voxels. Group of eight voxels are considered as little cubes, however good forms are obtained with isotropic voxels. The deformations are constrained to be locally one-to-one by ensuring that a tetrahedron never occupies any of the same volume as its neighbours. The vertices are moved iteratively until the best match is achieved.

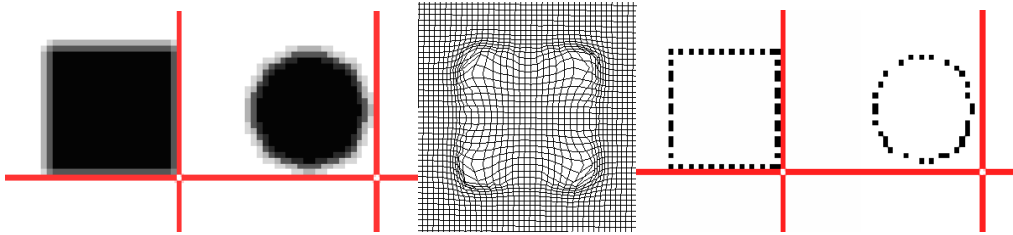


Figure 2 : Test case in 2D. Source image (case), template image (disc), transformation field between images, points in the space ('native nodes') to be warp with the same deformation field, moved points ('warped nodes') in align space.

### 3 MATERIALS AND METHODS

#### 3.1 Geometrical image data

In order to study the geometrical changes of the vascular wall, we used at first a pulsatile latex glove full of water with Gadolinium-based contrast agent. MR imaging was performed at several inflating levels. This experimental step include some general difficulties of our proposed post-processing method. After this preliminar phase, data from some patients and volunteers examinations were used to prove the feasibility in this study.

#### 3.2 MR data acquisition techniques

In this work, we chose to acquire all data sets in the same MRI system. MR imaging was performed on a 1.5-T system (Intera; Philips Medical Systems, Nederland, B.V). This constitutes a double advantage : Primo, the boundary conditions setup is optimal because the temporal (ECG) and spatial references are the same for all data sets. Secondo, the clinical application is easy because the patient undergoes all examinations into the same image protocol.

##### 3.2.1 Static geometry acquisition

The application of contrast agents in MR angiography is rapidly attracting more attention because of its simplicity in comparison with other types of MR angiographies<sup>1,6</sup>. Contrast-enhanced angiography (CE-MRA) relies on the shortening of the T1 relaxation time of blood due to the application of a Gadolinium-based contrast agent, and is relatively robust against artifacts. The result is an important contrast between blood and background. An arterial angiogram should not contain venous structures and must be therefore be acquired before the contrast agent reaches the veins. The delay time between arterial and venous enhancement then determines the maximum available acquisition time. This delay time can be quite short, requiring very fast acquisition methods based on the application of powerful gradient systems.

The image quality is excellent (higher specificity and sensitivity compared with Inflow and Phase Contrast Angiography sequences)<sup>6</sup> and allows us to extract a simple diastolic volume of interest with a spatial resolution next to 1,2x1,2x1,2 mm (isotropic voxel) for a 23 s breathhold.

A routine injected T1-FFE<sup>1</sup> sequence was applied in an oblique-sagittal direction in order to cover the whole aorta geometry (512x512x50) with a spatial resolution next to 1,2x1,2x1,2 mm (isotropic voxel) for a 23 s breathhold. This acquisition is triggered to the patient ECG, 430ms after R wave (in diastole). Analogue protocol was performed to the phantom (256x256x40) conserving the spatial resolution. After that the image segmentation gives the base for a static vascular mesh, inside which rigid model unsteady simulations can be assessed. But our work try to built a realistic model with dynamic wall.

### 3.2.2 Dynamic geometry acquisition

The objective of this acquisition is to track the real wall motion of vascular structures, observed previously in the static acquisition, but now, over the cardiac cycle. Here, the most important parameter is the spatial deformation from the first static geometry to the other cardiac phases.

True FISP imaging<sup>1,7</sup> (cine scans) are typically used to study wall motion and ventricular function. A variety of scan methods are available for cine scans. In this work we preferred retrospective triggered balanced TFE method (FFE), a True FISP imaging, because it has a number of advantages over other techniques (full coverage of the cardiac cycle, intrinsic high signal-to-noise ratio, high signal of blood, short repetition time (TR) and thus a short scan time and intrinsic flow compensation).

A balanced TFE sequence was applied in an oblique-sagittal direction in order to cover exactly the same field of view (FOV) of the first static acquisition, 256x256x25 for the patients and 128x128x20 for the phantom. So, the new isotropic voxel dimensions are next to 2.4x2.4x2.4 mm. Although this spatial resolution is not good, it is a good approximation to calculate the non linear transformation field necessary to build the moving meshes and it is also necessary to limit the examination time to one breathhold.

### 3.2.3 Velocity-encoded MR imaging and Pressure-encoded-MR imaging

A phase-contrast (PC) MR imaging<sup>1</sup> was performed orthogonal to the vessel axis in order to measure the velocity inlet profile at the ascending aorta. A velocity outlet at descending aorta is observed at the same time, but it is not always normal to the vessel axis. The reconstructed image gives hemodynamic informations (velocity, section area, flow rate, % regurgitation) of boundary condition related to the patient ECG. Other PC-MR images can be obtained into the vascular domain in order to validate CFD results. Pressure-gradients-encoded MR imaging

An acceleration-encoded MR imaging<sup>2</sup> was performed in an oblique-sagittal direction for estimate the pressure gradients into one slab paralel to the ascending aorta in order to estimates pressure gradients between inlet and outlets of the numerical domain. This is very usefull for the pressure outlets setup and permits the validation of the CFD results.

## 3.3 Post-processing

All of the next procedures described in this chapter were developed in-house in a Matlab language (The Matlabworks, Inc) with some C compiled routines (mexfiles) integrated to main sources. Some of them (affine coregistration and high dimensional warping are initially developed by John Ashburner<sup>5</sup> into SPM (statistical parametric mapping – University College London, 2000)<sup>8</sup>, an image processing toolbox dedicated to computational

neuroanatomy. The images was initially obtained in DICOM format and was converted to the Analyze-7 format (Mayo Clinic, Rochester, USA., <http://www.mayo.edu/bir/>) for filtering and non-linearar-transformation operations. The meshes was initially built in an ASCII format (\*.cas) into the Amira 3.0 environnement. The final set of moving meshes and hemodynamic boundary conditions will be exported into the correct AVBP format (CERFACS, Toulouse, France, <http://www.cerfacs.fr>) in order to perform CFD runs. Finally, all post-processing steps before CFD step was operated with a 2.80GHz processor with 1.5Go RAM. The geometrical post-processing operations are high lighted in the next diagram:

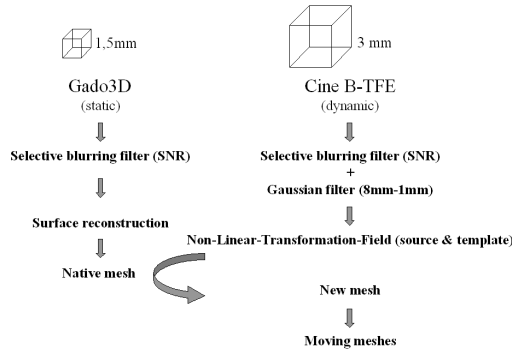


Diagram 1 : Post-processing steps

### 3.3.1 Filtering

MR image noise affects the post-processing algorithms. Filtering can be used to limit image noise but current filters reduce spatial resolution. In this work we applied a ‘selective blurring filter’ to all anatomical MR data (section 3.2.1 and 3.2.2). The filtered static data acquisition are submitted to 3D Level Set algorithm for a fine segmentation step. Compared to other classical filters, this filter achieves the best compromise between spatial resolution and noise reduction<sup>4</sup>. However, gaussian filtering is usefull in our proposed method : in order to reduce the chance of the algorithm being caught in the local minimum during the warping process, the first few iterations were carried out with the images (dynamic acquisition) smoothed using 8mm full width at half maximum gaussian convolution kernel. Last iterations have only the advantage of ‘selective blurring filter’ with a signal to noise ratio (SNR) equal to the intrinsic MR system noise (SNR~18 for this MR system). The homogeneous regions must have the ‘same’ gray level, so if the noise (gradient) is less than 2xSNR (95%), the ‘selective blurring filter’ apply a hard smooth (weighting=1). The treatment is different for the fine details where gradient is great than 2xSNR the filter gradually weight the smooth according to the image neighbours gradient (weighting=1/gradient).

### 3.3.2 Vascular 3D segmentation and ‘native’ mesh

After this stage of filtering, the anatomical surface can be extracted by means of level-set/fast marching methods<sup>3</sup> that accurately model the complex surfaces of pathological objects<sup>9</sup>. With the static geometry acquisition, the *level set* methods offer a highly robust and accurate method for tracking the interface in a volume of interest coming from the static MRI acquisition.

Given an initial position for an interface  $\Gamma$  (endovascular surface), where  $\Gamma$  is a closed surface in  $R^3$ , and a speed function  $F$  which gives the speed of  $\Gamma$  in its normal direction, the level set method takes the perspective of viewing  $\Gamma$  as a zero level set of a function  $f(x, t)$  from  $R^3$  to  $R$  whose evolution equation is :

$$\begin{aligned}\phi_t + F|\nabla\phi| &= 0, \\ \phi(x, t = 0) &= \text{given}\end{aligned}\tag{5}$$

This results in a set of binary data with exterior and interior (vascular) regions, tracking the position of endovascular wall.

### 3.3.3 Non linear transformation field - Moving meshes

Transforming one image volume to another involves estimating a spatial vector field (deformation field) that maps from coordinates of one volume to those of the other. In this work, one volume (the template volume) is considered as fixed, and a mapping from this image to the second volume (the source volume) is estimated. This approach to image transformation estimates the required spatial transformation at every voxel, and therefore requires many parameters. For example, to transform two volumes of size  $256^2 \times 25$  voxels, one needs 4 915 200 parameters ! The number of parameters describing the transformations exceeds the number of voxels in the data. Because of this, it is essential that the effective degrees of freedom are reduced by imposing priors or constraints on the transformation process. Bayesian statistics are used to incorporate a prior probability distribution into the warping model but at first, the pair of volumes were registered using a global registration method where differences in size and orientation between the volumes were removed by performing a 12-parameter affine transformation (translation, rotation, zoom and shear) in 3D<sup>5,10,11</sup>. This step is normally performed automatically by minimising (or maximising) mutual information of the images. This method provides a good starting point for estimating the optimum non-linear-transformation-field.

Initially, a value of four was used for the regularisation parameter ( $\lambda$ ), 15 iterations and 8mm for the gaussian smooth. After that,  $\lambda$  and smooth width are progressively reduced. The early iterations, with a ‘big’ regularisation parameter are necessary to find the low frequency warping (big movements) and obtain a smooth transformation field, last iterations, with a ‘little’  $\lambda=0.5$  are necessary to come to fine warping (details). The complete process took about 200 iterations and delay 2 hours to estimate the 4 915 200 parameters on the current CPU processor. All the data could be stored in memory. The native mesh is transformed node by node with the same non-linear-transformation-field to obtain the new mesh related to the delay time between template and MRI source volumes. Other meshes be obtained by means of the same spatial process between respective delay and successive sources and templates volumes. This method have the advantage to conserve the same number of nodes and connectivities in all meshes, where only node coordinates are modified. This is necessary to ALE formulation in CFD algorithms and has the potential to do only one segmentation step for obtain the ‘native’ surface reconstruction and the ‘native’ mesh. After that, only spatial transformations are applied to simulates the real vascular movement.

### 3.4 Non coupled numerical method - fluid to wall interaction

A first numerical model was developed<sup>12</sup> in order to assess the wall shear stress changes after endovascular stenting. In this approach, the fully coupled fluid–structure problem is replaced by a simpler fluid problem with moving boundaries. The Navier–Stokes equations were solved numerically with an appropriate finite-element-based method which handles time-dependent geometries. The main result supports the idea that stenting can induce endothelial dysfunction via haemodynamic perturbations. From this study, which enabled us to check the feasibility of an uncoupled CFD, we widened the problem with the more complex case of vascular geometries. From non-linear-transformation results, the set of successive meshes are prepared to the ALE formulation into the AVBP Navier-Stokes code.

The feasibility of the proposed method is tested initially with phantom results and after with real vascular results. The basic test consists of a dynamic ‘move mesh only’ run without hemodynamic influence.

This paper propose a protocol to do complete CFD runs where the velocity and pressure boundary conditions are considered but our preliminar results only gives the answer of the moving meshes process.

## 4 RESULTS

### 4.1 Filtering MR Data

All geometric MR images are filtered with the ‘selective blurring filter’. The filtering preserve vascular contours and hardly smooth interior and exterior vascular domain (Figure 3). Is optimal to the segmentation algorithm which must track the native wall interface. After that, and only for dynamic images, gaussian filtering step allow the start of warping process. Successive 8mm, 6mm, 4mm and 2mm full width at half maximum gaussian convolution kernel are performed between each level of regularisation constant ( $\lambda$ ). The patient’s images present an aortic coarctation (see arrows in f).

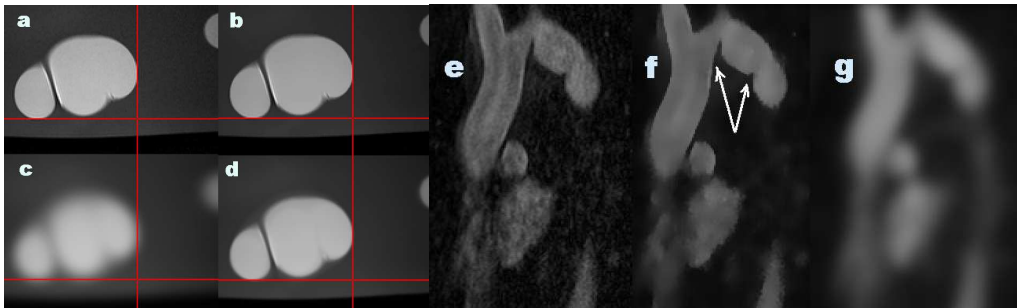


Figure 3 : Native phantom’s transverse image (a), with selective blurring filter (SNR=15 and 9x9 convolution matrix) (b), with selective blurring filter + gaussian filter ( 8mm full width at half maximum gaussian convolution kernel) (c) and the same with gaussian at 2 mm width. Native patient’s CE-MRA oblique sagittal image (e), with selective blurring filter (SNR=18 and 9x9 convolution matrix) (f), gaussian filter with 8mm full width at half maximum gaussian convolution kernel + selective blurring filter (g).

### 4.2 ‘Native’ mesh

Figure 4 illustrates the results of described treatment for phantom’s and patient’s study. The respective surface generation is visually assessed by the operator with native images superposition option into interactive 3D window. First static tetrahedral mesh, the ‘native mesh’, is manufactured into the Amira 3.0 environnement<sup>13</sup>. The output is an ASCII file (\*.cas) containing the node coordinates and connectivities of ‘native’ source mesh and readable by the CFD and post-processing softwares.

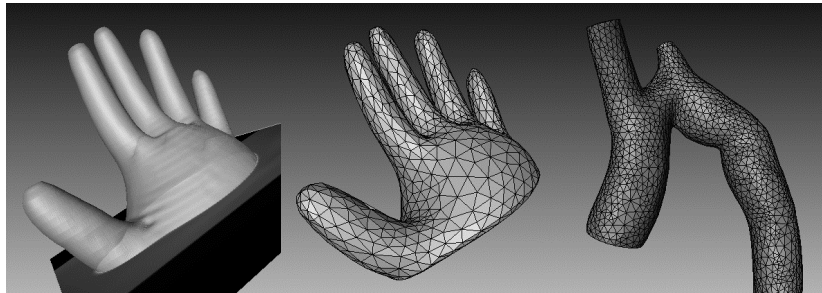


Figure 4: Phantom surface reconstruction , ‘native’ phantom mesh (6656 tetrahedrons) and ‘native’ patient mesh (42163 tetrahedrons).

### 4.3 Non-linear-transformaton-field estimation

Before warping, an alignment step is necessary to find a good starting point for estimating the optimum non-linear-transformation-field. Some methods are available but we choose the mutual information of the volume histogram for our study. Ideally, the graph representing two identical volumes at the form *vol1* function of *vol2* is a line of the type  $x=y$ . Graph between *source* and *template* volumes represents the shape of mutual histograms (Figure 5). Alignment of these two volumes try to reduce this shape into line tracing  $source=template$ .

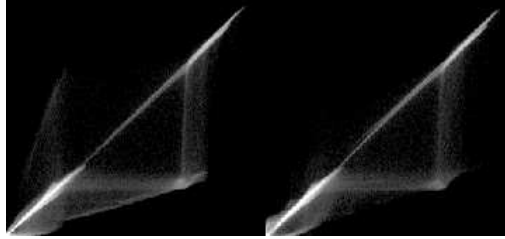


Figure 5 : Original mutual histograms (left) and final mutual histograms (right) of template's voxel intensities function of source's voxel intensities.

Affine (rigid) transformation is often expressed as a simple matrix multiplication ( $y=\mathbf{R}x$ ), where  $\mathbf{R}$  resumes translations, rotations, zoom and shears values of the transformation. For the example presented in this paper,  $\mathbf{R}$  have the next values where diagonal values indicates the actual spatial resolution :

$$R = \begin{bmatrix} 2,42 & 0,00 & -0,15 & -100,88 \\ -0,00 & 2,42 & 0,01 & -98,21 \\ 0,02 & -0,00 & 2,42 & -82,95 \\ 0 & 0 & 0 & 1,00 \end{bmatrix}$$

Matrix  $\mathbf{R}$  and trilinear interpolation is used to write the new volume (Figure 6). Only  $\mathbf{R}$  is useful to the warping process, writed volume is here as an explicative element.

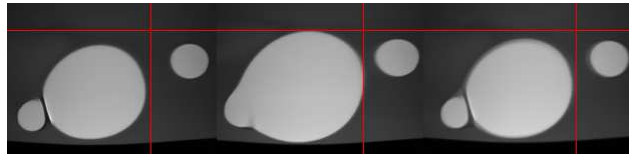


Figure 6: The phantom's images at two inflating levels. The images present a transverse section towards the middle of the volume. Source (left), template (middle) and transformed source (right) volumes. Crosshairs indicates the same spatial coordinate.

Source and the template volumes are smoothed with an 8mm gaussian filter,  $\mathbf{R}$  is loaded,  $\lambda$  is set to 4 and the algorithm work for 10 iterations. After that, the warping process continue for 180 iterations, regularisation constant and filter width decreases gradually to  $\lambda=0.5$  and 2mm. The Algorithm took about 5 hours for this example. Figure 7 illustrates two volumes, their corresponding deformation field and their final jacobian values (determinant). The symmetry of the registration process was examined by repeating the warping process swapping the source and template volumes. This gave a second deformation field, which, if the registration procedure is symmetric, should be the inverse of the first. Image of jacobian determinant represents the relative changes of voxels volume. Some interpolation and warping errors appears in inverse image.

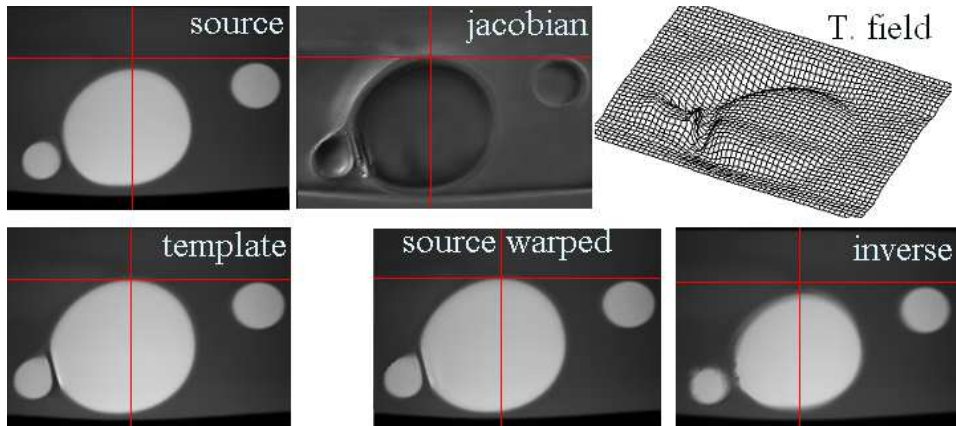


Figure 7: Phantom's images and reconstructed phantom's images by means of the non-linear-deformation-field.

Two patient's dynamic image volumes are processed following the same method presented before. The two volumes are initially aligned and warped into a process who took about 6 hours for 242 iterations. Figure 8 illustrates two cardiac phases of an aortic coarctation, note that aortic root has an important shifting and envascular diameter is increased.

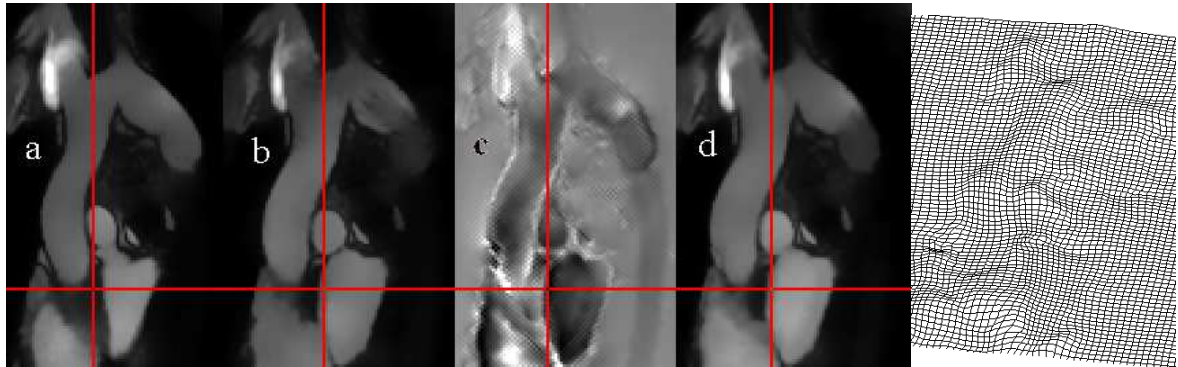


Figure 8: Two cardiac phases of aortic coarctation (a,b), their jacobian determinant image (relative volume changes)(c), the reconstructed image and the deformation field. Delay time=250 ms.

#### 4.4 Moving meshes

The movement of the mesh is independent of the numerical method. However, the grid position must to be known for each node at each time step. The movement of the mesh is supposed to be linear during a timestep  $\Delta t$  so that the grid speed is piecewise constant. The ALE formulation allows the time interpolation between a few meshes coming from cardiac phases, so all timesteps  $\Delta t$  of a CFD are calculated into the AVBP code. Figure 9 illustrates the native and the second phase of the latex glove. The analogous case is presented for the vascular meshes of aortic coarctation.

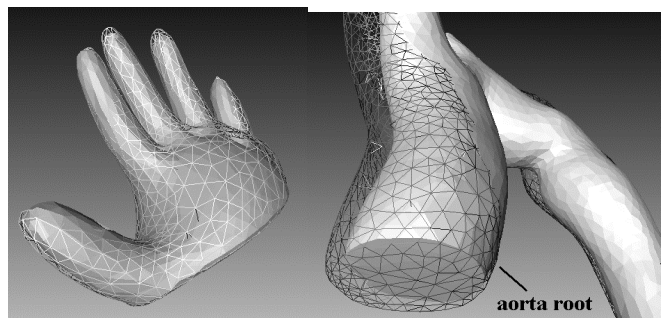


Figure 9 : Native (shaded) and warped (lines) meshes of phantom and patient's volumes

#### 4.5 Velocity-encoded MR data

Transverse phase-contrast (PC) MR imaging<sup>1</sup> was performed on the patient with aortic coarctation. The reconstructed image (Figure 10) illustrates two vascular sections in the same transverse plane, at systolic pic. On top the ascending aorta, on bottom its descending segment. The pixel intensities represents the normal (to the plane) velocities, which is positive to the white levels (to the observer) and negative to the black levels. Gray level corresponds to the static structures (the zero). This information has the advantage of allowing some quantitative hemodynamics evaluations. The post-processing operations are possible because the vascular wall position is knowed, the limits of the ascending and descending sections are defined and the flow is perpendicular to the ascending section (velocity inlet of computational domain). Here, the descending section is perpendicular to the flow, but it is not true everytime. The graph illustrates the velocity evolution function of cardiac delays for the ascending aorta. Stroke volume, and another hemodynamic information are availables from this MR acquisition.

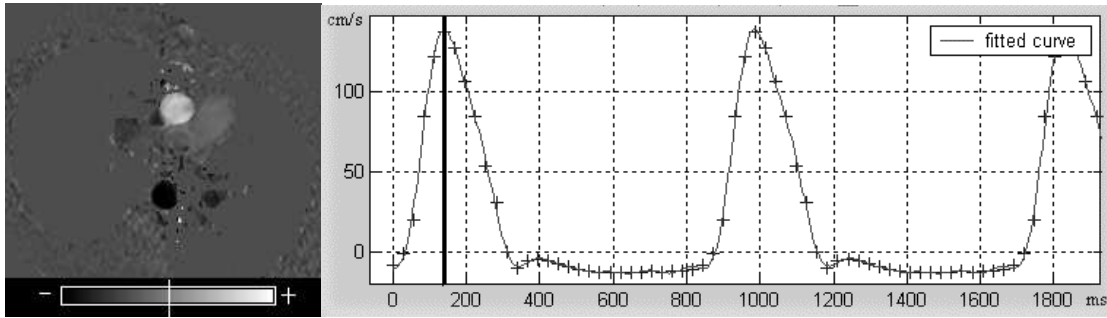


Figure 10 : Reconstructed PC-MR velocity (left) and graph of fitted velocity (mean) function in the ascending aorta (right).

In order to impose the inlet velocity to the boundary condition patch at the aortic's root, the velocity data set are converted on a function (6) of time by means of a fourrier fitting with 7 harmonics. This post-processing is automatic from data set to final velocity function. Here, only means velocities (throughout the section) are presented, but maximum and minimum velocities, area and flow rate are available to the numerical analysis. The general Fourier model is :

$$cf(x) = a_0 + a_1 \cos(x*w) + b_1 \sin(x*w) + \dots + a_7 \cos(7*x*w) + b_7 \sin(7*x*w) \quad (6)$$

a0 =	19.12 (18.72, 19.53)	w =	0.007434 (0.00743, 0.007438)
a1 =	16.95 (16.26, 17.63)	b1 =	50.81 (50.21, 51.4)
a2 =	-26.24 (-26.92, -25.56)	b2 =	25.05 (24.36, 25.74)
a3 =	-19.84 (-20.44, -19.24)	b3 =	-7.153 (-7.871, -6.435)
a4 =	-2.518 (-3.13, -1.906)	b4 =	-7.234 (-7.813, -6.655)
a5 =	-1.97 (-2.564, -1.376)	b5 =	-4.244 (-4.824, -3.663)
a6 =	2.006 (1.397, 2.615)	b6 =	-4.456 (-5.04, -3.872)
a7 =	2.29 (1.714, 2.867)	b7 =	-0.3239 (-0.9123, 0.2645)

Table 1: Coefficients of general Fourier model with 95% confidence bounds.

#### 4.6 Pressure-encoded MR data

Pressure gradient maps of the thoracic aorta of a volunteer was performed in the same MR system type by Jean-Pierre Tasu<sup>2</sup> at the C.I.E.R.M., ESA 8081-CNRS, Université Paris-Sud, Le Kremlin Bicêtre, France. Figure 11 presents an image where a gray scale is applied, with the high pressure gradient in white and the low one in black. Arrows represent the direction of the pressure gradient vector where the gray scale represents the gradient values. The absolute

value of the pressure gradient is also indicated by the length of the arrows. The time after the R-waves (ECG) is known.

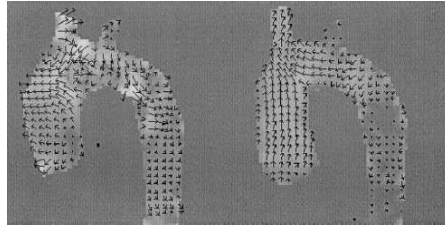


Figure 11: Pressure gradient maps of the thoracic aorta of a volunteer.

## 5 DISCUSSION & CONCLUSION

Algorithm does not guarantee that the optimum solution will be achieved, but it does mean that a local optimum solution can be reached. Robust optimisation methods that almost always find the global optimum would take an extremely long time to run with a model that uses millions of parameters. These methods are simply not feasible for routine use on problems of this scale. The correct management of regularisation constant and filters during warping process allows the algorithm to find the solution.

Spatial resolution is actually limited by technical restrictions in cine scans imaging and this is the reason why contrast enhanced acquisition is proposed. Dynamic study to a lesser degree is here a trick to supply motion to native mesh, created by means of better resolution. Our proposed method presents the advantage of impose the realistic position of the wall to the numerical problem, without having to make incorrect assumptions about vessel's rheology response. However, it can be limited for high volume changes (ventricular study) because little elements near to high elements origin numerical mismanagements. In general the use of mesh adaptation techniques is motivated by the demand to optimize the resolution of flow calculations. Often one does not know a priori exactly where to cluster additional points in order to better resolve the physical phenomena of interest. It is therefore necessary to determine this automatically during the calculation by using flow sensors. But here, the mesh adaptation is additionnally motivated by volume changes before any numerical application. One solution is to compute grid refinements based on the solution fields computed by AVBP in the native mesh and selected quantities serve as flow sensor to detect important gradients in the flow. The refinement methods of HIP are applied to AVBP<sup>14</sup>. But before that, another solution is to correct the shape of each mesh by smoothing node distances without any connectivity change (mmg3D, INRIA, FR). Excepting all methodological details, the method gives a direct way to impose realistic wall interaction to hemodynamic time boundary conditions, from medical examinations performed into a simple MR protocol. Preliminar methods presented in this paper have some difficulties to move fine intimal flap structure observed in aortic dissection but is just the process to simulates aorta root movements or aortic compliance changes. The aortic root motion has a direct impact on the mechanical stresses acting on the aorta. As an aortic aneurysm dilates, the longitudinal stresses in the bulb rises significantly and may cause rupture<sup>15,16</sup>. In other respects, it is clear from the clinical literature that parametric alterations within a single treatment, or relying on the gradual empirical modifications of these treatments, will only modestly increase the life expectancies of patients with aortic coarctation. Alternatively, more favorable long term results may be possible by examining the origin of coarctation symptoms that emanate from alterations in vascular hemodynamics within the ascending aorta.

## Acknowledgements

The authors gratefully acknowledge the assistance of Gwenael Herigault (MR Clinical Scientist, Philips Medical Systems-France) and the collaboration of Pascal J Frey for mmg3D (INRIA-France).

Special acknowledgements to CINES for available time at parallel scientific calculation systems and to CERFACS staff for its help on numerical methods.

## REFERENCES

- [1] M T Vlaardingerbroek and J A Den Boer, *Magnetic Resonance Imaging – Theory and practice*, Springer-Verlag Berlin Heidelberg New York, 3<sup>rd</sup> Ed, 321-371 (2004).
- [2] J P Tasu, E Mousseaux, J Bittoun, *Estimation of pressure gradients in pulsatile flow from magnetic resonance acceleration measurements*, *Magnetic Resonance in Medicine*, 2000;44 :66-72 .
- [3] J A Sethian, *Level Set Methods and Fast Marching Methods*, Cambridge University Press (1999).
- [4] D Gensanne, G Josse and D Vincensini, *A post-processing method for multiexponential spin-spin relaxation analysis of MRI signals*, *Physics in Medicine and Biology*, 2005;50: 1-18 .
- [5] J Ashburner, J L R Andersson, and K J. Friston, *High-Dimensional Image Registration Using Symmetric Priors*, *NeuroImage* 1999;9:619–628 .
- [6] Contrast Enhanced MR Angiography, *Methods, Limitations and possibilities*, M Kouwenhoven, *Acta Radiologica*, 1997;38 .
- [7] M. Deimling, O. Heid, *Magnetization prepared True FISP Imaging*, Proc. 2nd Ann. Meeting ISMRM, San Francisco, 1994;495 .
- [8] [www.fil.ion.ucl.ac.uk/spm/doc/theses/john/](http://www.fil.ion.ucl.ac.uk/spm/doc/theses/john/)
- [9] T. Deschamps, *Vessel segmentation and blood flow simulation using Level-Sets and Embedded boundary methods*, *International Congress Series*, 2004;1268: 75– 80 .
- [10] Eddy, W. F., Fitzgerald, M., & Noll, D. C.. *Improved Image Registration by Using Fourier Interpolation*, *Magnetic Resonance Imaging*, 1996;36: 923-931.
- [11] Cox, R. W., & Jesmanowicz, *Real-Time 3D Image Registration for Functional MRI*, *Magnetic Resonance in Medicine*, 1999;36, 923-931 ().
- [12] F. Nicoud, H. Vernhet, M. Dautat, *A numerical assessment of wall shear stress changes after endovascular stenting*, *Journal of Biomechanics*, 2005; 38:2019–2027.
- [13] [www.amiravis.com](http://www.amiravis.com)
- [14] Müller J.-D., Schönfeld, T., and Rudgyard, M. *A comparison of the treatment of hanging nodes for hybrid grid refinement*. In 13th Computational Fluid Dynamics Conference (Snowmass, USA, 1997), pp. AIAA Paper 1997–1859.
- [15] Thubrikar MJ, Agali P, Robicsek F, et al. *Wall stresses as a possible mechanism for the development of transverse intimal tears in aortic dissections*. *J Med Eng Technol*. 1999; 23: 127-134
- [16] Beller CJ, Labrosse MR, Thubrikar MJ, et al. *Role of aortic root motion in the pathogenesis of aortic dissection*. *Circulation*. 2004;109:763-769.